



# Chemodynamical Analysis of Metal-rich High-eccentricity Stars in the Milky Way's Disk

Ayeon Lee<sup>1</sup> , Young Sun Lee<sup>2,3</sup> , Young Kwang Kim<sup>2</sup> , Timothy C. Beers<sup>3</sup> , and Deokkeun An<sup>4</sup> <sup>1</sup>Department of Astronomy, Space Science, and Geology, Chungnam National University, Daejeon 34134, Republic of Korea<sup>2</sup>Department of Astronomy and Space Science, Chungnam National University, Daejeon 34134, Republic of Korea; [youngsun@cnu.ac.kr](mailto:youngsun@cnu.ac.kr)<sup>3</sup>Department of Physics and Astronomy and JINA Center for the Evolution of the Elements, University of Notre Dame, IN 46556, USA<sup>4</sup>Department of Science Education, Ewha Womans University, Seoul 03760, Republic of Korea

Received 2022 October 7; revised 2023 January 23; accepted 2023 January 27; published 2023 March 22

## Abstract

We present a chemodynamical analysis of 11,562 metal-rich, high-eccentricity halo-like main-sequence stars, which have been referred to as the Splash or Splashed Disk, selected from the Sloan Digital Sky Survey and Large Sky Area Multi-Object Fiber Spectroscopic Telescope. When divided into two groups, a low- $[\alpha/\text{Fe}]$  population (LAP) and a high- $[\alpha/\text{Fe}]$  population (HAP), based on kinematics and chemistry, we find that they exhibit very distinct properties, indicative of different origins. From a detailed analysis of their orbital inclinations, we suggest that the HAP arises from a large fraction ( $\sim 90\%$ ) of heated disk stars and a small fraction ( $\sim 10\%$ ) of in situ stars from a starburst population, likely induced by interaction of the Milky Way with the Gaia-Sausage/Enceladus (GSE) or another early merger. The LAP comprises about half accreted stars from the GSE and half formed by the GSE-induced starburst. Our findings further imply that the Splash stars in our sample originated from at least three different mechanisms: accretion, disk heating, and a merger-induced starburst.

*Unified Astronomy Thesaurus concepts:* [Milky Way Galaxy \(1054\)](#); [Milky Way disk \(1050\)](#); [Milky Way dynamics \(1051\)](#); [Milky Way formation \(1053\)](#); [Milky Way evolution \(1052\)](#); [Stellar abundances \(1577\)](#); [Stellar dynamics \(1596\)](#); [Stellar populations \(1622\)](#)

## 1. Introduction

The early Milky Way (MW) experienced a chaotic assembly history due to various mergers with small- and large-scale satellites. To understand the complex accretion history of the MW, it is necessary to study these past merger events in detail. Because the physical properties (mass, star formation history, orbital properties, etc.) of a dwarf galaxy that has merged with the MW are trackable from its disrupted stars, investigation of their chemical and kinematic properties provides an understanding of the MW merger history. Recently, great advances have been made in Galactic Archaeology—the study of the formation and assembly history of the MW—thanks to the advent of large photometric and spectroscopy surveys such as the legacy Sloan Digital Sky Survey (SDSS; York et al. 2000), the Sloan Extension for Galactic Understanding and Exploration (SEGUE; Yanny et al. 2009; Rockosi et al. 2022), the Large sky Area Multi-Object Fiber Spectroscopic Telescope (LAMOST; Luo et al. 2015), the Apache Point Observatory Galactic Evolution Experiment (APOGEE; Majewski et al. 2017), GALactic Archaeology with HERMES (GALAH; De Silva et al. 2015), and others, along with accurate astrometry and radial velocities from a series of Gaia data releases (DRs; Gaia Collaboration et al. 2016, 2018, 2021, 2022).

The large-survey data have enabled the identification of not only numerous small-scale accretion events (Myeong et al. 2018, 2019; Kim et al. 2019; Kwang Kim et al. 2021; Koppelman et al. 2019; Naidu et al. 2020; Necib et al. 2020; Yuan et al. 2020; An & Beers 2020, 2021, 2021; Horta et al. 2021; Re Fiorentin et al. 2021) but also at least one significant merger event, known as Gaia-Sausage and -Enceladus (GSE;

Belokurov et al. 2018; Helmi et al. 2018), all of which have contributed to building up the MW. Note that there is an argument for an additional massive accretion event (“Kraken”) inferred from globular clusters near the center of the MW, which is older than the GSE (Kruijssen et al. 2019).

Cosmological zoom-in simulations predict that the GSE merger occurred 8–11 Gyr ago, with a progenitor mass of about  $10^9$ – $10^{10} M_{\odot}$  (Belokurov et al. 2018; Mackereth et al. 2019). The GSE merger significantly restructured the stellar populations of the MW, and a range of distinct stellar populations emerging from the GSE merger event have been discovered. One example among them is the recognition of a large fraction of accreted stars from the GSE in the local halo. This population exhibits very strong radially dominated orbits with eccentricity ( $e$ ) larger than 0.8–0.9 (Chiba & Beers 2000; Belokurov et al. 2018; Deason et al. 2018; Mackereth et al. 2019), low rotation velocity (or even retrograde motion), and a large spread in chemical abundances (Helmi et al. 2018; Mackereth et al. 2019).

The GSE merger event also may have influenced the formation and evolution of the Galactic disk by dynamically heating the proto-disk of the MW and triggering star formation. As evidence of this, numerous studies (e.g., Nissen & Schuster 2010; Hawkins et al. 2015; Bonaca et al. 2017; Haywood et al. 2018; Fernández-Alvar et al. 2019) have identified a large fraction of metal-rich ( $[\text{Fe}/\text{H}] > -1.0$ ), high-eccentricity, halo-like stars with low angular momentum ( $V_{\phi} < 100 \text{ km s}^{-1}$ ) and high levels of  $[\alpha/\text{Fe}]$ . Because these stars exhibit kinematics and chemistry somewhat similar to those of the thick disk, they are regarded as proto-disk stars heated by merger events, which became in situ local halo stars (Nissen & Schuster 2010; Bonaca et al. 2017; Haywood et al. 2018; Di Matteo et al. 2019).

Belokurov et al. (2020) carried out a more extensive analysis of these stars, which possess high metallicity ( $-0.7 < [\text{Fe}/\text{H}] < -0.2$ ),

low angular momentum, and high-eccentricity orbits, and found that this population of stars, which they named “Splash,” has a chemistry and kinematics distinct from those of other known stellar populations in the MW. It has further been shown that the Splash stars have the characteristics of high- $[\alpha/\text{Fe}]$  and high-velocity dispersion (Nissen & Schuster 2010; Hawkins et al. 2015; Haywood et al. 2018; Di Matteo et al. 2019; Belokurov et al. 2020), which somewhat resemble those of the thick disk. However, there are some discrepancies as well; the Splash stars exhibit lower angular momentum (or even retrograde motions) and higher eccentricity ( $e > 0.5$ ) than thick-disk stars. Nonetheless, there appears to exist a smooth transition between the Splash and the thick disk in terms of rotation velocity ( $V_\phi$ ),  $[\alpha/\text{Fe}]$ , and ages. A series of chemodynamical properties have pointed to a situation where the Splash stars were born in the proto-disk of the MW, and later their orbit was altered by dynamical heating from massive ancient accretion events such as the GSE (e.g., Bonaca et al. 2017; Haywood et al. 2018; Di Matteo et al. 2019; Gallart et al. 2019).

The above claim is advocated by various hydrodynamical simulations (e.g., Belokurov et al. 2020; Grand et al. 2020; Dillamore et al. 2022). For example, from magnetohydrodynamic simulations, Grand et al. (2020) demonstrated that the GSE event was a gas-rich merger, which results not only in a starburst that rapidly forms a compact, rotationally supported thick disk, but also the dynamical heating of the proto-disk of the MW—altering its constituent stars to become more eccentric and to have lower angular momenta, eventually bridging between the thick disk and inner halo populations of the MW.

On the contrary, a hydrodynamical simulation by Amarante et al. (2020) demonstrated that a clumpy isolated galaxy could reproduce the Splash-like stars, whose kinematic and chemical properties are similar to those observed in the MW without a major merger via scattering of the formed clumps. Based on this, Amarante et al. (2020) argued that the thick disk and Splash could arise from the same process, and that the Splash is merely represented by the low tail of the angular-momentum distribution of the thick-disk population, because both populations exhibit smooth transitions in kinematics, age, and chemistry in their simulation.

As described above, there have been many studies carried out related to the origin of the metal-rich, high- $[\alpha/\text{Fe}]$ , and halo-like kinematic population. Nevertheless, it is still a matter of debate. Moreover, even though there also exists a low- $[\alpha/\text{Fe}]$  population in the Splash region, only a few studies have been carried out to pin down its origin (e.g., Zhao & Chen 2021; Myeong et al. 2022). Besides, hydrodynamic simulations (e.g., Grand et al. 2020) predict an additional stellar population formed from a starburst due to a GSE-like merger in the Splash region; this population mostly occupies a relatively low- $[\alpha/\text{Fe}]$  region in the  $[\alpha/\text{Fe}]$ – $[\text{Fe}/\text{H}]$  plane. Recently, An et al. (2023) announced the discovery of such a starburst event, which they termed the “Galactic Starburst Sequence (GSS),” from study of a large photometric data set with available Gaia proper motions and parallaxes. Considering this, it is worthwhile to explore the possible interconnection between the low- $[\alpha/\text{Fe}]$  stars and the GSE, and the starburst population that the GSE merger may have produced.

In this study, we first identify Splash stars from a large number of main-sequence (MS) and main-sequence turnoff (MSTO) stars from SDSS and LAMOST confined to  $|Z| < 3.0$  kpc. After separating this sample into two groups,

based on chemistry and velocity dispersions, we search for distinct kinematic and chemical behaviors between them. Because previous studies mostly utilized giants or MSTO stars, our MS/MSTO sample may provide a different perspective on the chemodynamical properties of the Splash stars.

This paper is organized as follows. In Section 2, we describe the selection of F-, G-, and K-type MS/MSTO stars from SDSS and LAMOST, and how we combine the two data sets. In Section 3, we calculate space velocity components and orbital parameters of our program stars. Section 4 describes how we select the Splash stars, and how we divide them into low- $[\alpha/\text{Fe}]$  and high- $[\alpha/\text{Fe}]$  populations. Section 5 presents our findings; implications are considered in Section 6. Section 7 summarizes our results.

## 2. The Sample of MS and MSTO Stars

We selected the sample of stars used in this study from SDSS and LAMOST. In this section, we describe how we selected them from the two survey data sets.

### 2.1. The SDSS Sample

The SDSS sample consists of stellar objects not only from the main legacy SDSS survey but also its subsurveys—namely SEGUE, the Baryon Oscillation Spectroscopic Survey (BOSS; Dawson et al. 2013), and the extended Baryon Oscillation Spectroscopic Survey (eBOSS; Blanton et al. 2017). Low-resolution ( $R \sim 1800$ ) stellar spectra from these surveys were processed through a recent version of the SEGUE Stellar Parameter Pipeline (SSPP; Allende Prieto et al. 2008; Lee et al. 2008a, 2008b, 2011a; Smolinski et al. 2011) to deliver accurate stellar atmospheric parameters such as effective temperature ( $T_{\text{eff}}$ ), surface gravity ( $\log g$ ), and metallicity parameterized by  $[\text{Fe}/\text{H}]$ , as well as  $[\alpha/\text{Fe}]$  and  $[\text{Mg}/\text{Fe}]$ . The reported typical errors of the estimated parameters are 180 K in  $T_{\text{eff}}$ , 0.24 dex in  $\log g$ , 0.23 dex in  $[\text{Fe}/\text{H}]$ , and  $< 0.1$  dex for  $[\alpha/\text{Fe}]$  and  $[\text{Mg}/\text{Fe}]$ . The SSPP also has the capability to estimate  $[\text{C}/\text{Fe}]$ ,  $[\text{N}/\text{Fe}]$ , and  $[\text{Na}/\text{Fe}]$  (see Lee et al. 2013; Kim et al. 2022; Koo et al. 2022 for more details) from SDSS-like low-resolution stellar spectra.

In this SDSS sample, we did not include stars that belong to spectroscopic plug-plates of open cluster and globular cluster fields, to minimize contamination by cluster member stars. For stars that were observed multiple times (often calibration objects), we included only the spectrum with the highest signal-to-noise ratio (S/N). Furthermore, we visually inspected the spectra of the selected stars in order to exclude white dwarfs and objects with defective spectra that could deliver incorrect stellar parameters. This sample is dominated by the objects observed by SEGUE, because its science goals and survey design were specific to the study of the stellar populations in the MW.

### 2.2. The LAMOST Sample

The LAMOST stars in our sample come from LAMOST Data Release 5 (DR5; Luo et al. 2019), which provides more than 5 million stellar spectra. Thanks to the similar wavelength coverage (3800–9000 Å) and resolution ( $R \sim 1800$ ) of the stellar spectra, the SSPP is readily applicable to the LAMOST stellar spectra to determine the stellar atmospheric parameters as well as  $[\alpha/\text{Fe}]$  and  $[\text{Mg}/\text{Fe}]$  (see Lee et al. 2015 for details).

Because the target selection for LAMOST is based on various photometric data, and we require  $g_0$ ,  $r_0$ , and  $i_0$ -band magnitudes to run the SSPP, we cross-matched the LAMOST DR5 data with AAVSO Photometric All-Sky Survey Data Release 10 (APASS DR10; Henden et al. 2018) for the objects in LAMOST DR5. We employed extinction values from Wang et al. (2016) to correct for the reddening of each star, and we ran the SSPP on the LAMOST spectra with the reddening-corrected APASS photometry.

It is recognized that LAMOST DR5 includes a non-negligible number of poorly flux-calibrated and defective spectra, which can result in incorrect estimated stellar parameters and chemical abundances. Since it is not realistic to visually inspect over five million spectra, we devised a scheme to identify and remove such spectra, as described below.

For a well-flux-calibrated spectrum, the shape of an observed spectrum closely follows that of a synthetic spectrum generated with the estimated  $T_{\text{eff}}$ ,  $\log g$ , and  $[\text{Fe}/\text{H}]$  from the SSPP. It should also be noted that the flux of the generated synthetic spectrum was rescaled to that of the observed spectrum. In the case that the observed spectrum does not mimic the synthetic spectrum, the wavelength ( $\lambda_{\text{max}}$ ) at which the peak of the pseudo continuum flux occurs is different between the observed and synthetic spectra. Additionally, there are large flux differences at the peak wavelengths. Following this reasoning, we compared the  $\lambda_{\text{max}}$  and flux differences, to determine whether or not the observed spectrum matches the model spectrum well. After several experiments, we decided to exclude stellar spectra whose  $\lambda_{\text{max}}$  value between the observed and model spectrum differs by 1000 Å and whose flux difference at  $\lambda_{\text{max}}$  differs by over 40% between them. In addition to these criteria, we eliminated spectra that exhibit flux differences at  $\lambda_{\text{max}}$  larger than 50% between the observed and model spectrum, even if the difference in  $\lambda_{\text{max}}$  is less than 1000 Å. Application of these criteria removed 7.6% of the LAMOST spectra. As a final step, we visually inspected these stars to ensure that they were not erroneously removed from the list. Similar to the SDSS sample selection, we chose to use the spectrum with the highest-S/N spectrum for multiply observed stars.

### 2.3. Combining the SDSS and LAMOST Samples

The SDSS and LAMOST stellar sources are complementary to each other in the sense that the LAMOST stars are mostly brighter than  $r_0 < 17$  (~90%), whereas the SDSS stars cover the magnitude range  $r_0 = 14$ –21. A wide range of stellar magnitudes probe different regions of the MW, and having a large number of homogeneously sampled stars enables us to explore the kinematic and chemical properties of various stellar populations. Thus, it is desirable to combine the SDSS and LAMOST stellar samples, with their available stellar parameters and chemical abundances derived from the SSPP.

Given the similar spectral coverage and resolution of the SDSS and LAMOST spectra, it is expected that the random and systematic errors in the derived stellar parameters and chemical abundances will also be similar. Nonetheless, owing to subtle differences in the instrumental data acquisition systems between the two surveys, there may exist systematic difference in stellar parameters and chemical abundances delivered by the SSPP as well as in the radial velocities (RVs), which we need to check for before combining the different data sets.

To check for systematic differences in the stellar parameters and chemical abundances, we made use of about 21,000 stars in common between the SDSS and LAMOST. We found the mean offsets of 9 K, 0.1 dex, 0.1 dex, 0.01 dex, and 0.01 dex for  $T_{\text{eff}}$ ,  $\log g$ ,  $[\text{Fe}/\text{H}]$ ,  $[\alpha/\text{Fe}]$ , and  $[\text{Mg}/\text{Fe}]$ , respectively. Because they are smaller than the measured uncertainty ranges, we did not correct for the systematic offsets in the stellar parameters and chemical abundances.

Concerning the systematic offset in the RVs, because we employ the Gaia proper motions to compute the stellar space velocity, we decided to put the radial velocities of SDSS and LAMOST stars on the same Gaia scale. We obtained a systematic offset of  $+4.9 \text{ km s}^{-1}$  in RV from stars in common between LAMOST and Gaia Early Data Release 3 (EDR3; Gaia Collaboration et al. 2021), and added its offset value to the RV derived from LAMOST. Only a small number of SDSS stars in common with the Gaia data had reported RVs from Gaia, owing to their faintness. Thus, as an alternative, we adjusted the RVs of the SDSS stars to the Gaia scale by using the stars in common between SDSS and LAMOST with corrected RV with Gaia. The systematic difference found was  $+5.1 \text{ km s}^{-1}$ , and we corrected the SDSS RVs by this amount.

We also checked the photometric distance estimates used for the SDSS and LAMOST samples, to ensure an accurate calculation of the space velocity. The photometric distance of the SDSS stars used in this study was derived following the methods of Beers et al. (2000, 2012), whereas that of the LAMOST stars, which was computed by Wang et al. (2016), was taken from the value-added catalog of LAMOST DR5 (Xiang et al. 2019). We compared the distances of SDSS and LAMOST stars with their parallax-based distance estimates available from Gaia EDR3, after correcting for the reported zero-point offset of  $-0.017 \text{ mas}$  (Lindgren et al. 2021). Only stars with whose relative parallax errors smaller than 10% were used for this exercise. We found that the distance modulus (DM) of the SDSS stars was smaller than the DM of Gaia by  $-0.031 \text{ mag}$ , while we found a systematic difference of  $-0.001 \text{ mag}$  for the DM for LAMOST. We corrected both samples for these systematic differences.

To obtain the combined set of MS and MSTO stars from the SDSS and LAMOST samples, we applied the following conditions: the stellar spectra had to have  $S/N > 10$ , averaged over 4000–8000 Å,  $7 < g_0 < 20.5$ ,  $0 < (g - r)_0 < 1.2$ ,  $\log g > 3.5$ , and  $4400 < T_{\text{eff}} < 7000 \text{ K}$ . Based on previous experience, these S/N, color, and temperature cuts ensure accurate estimates of stellar parameters and chemical abundances.

## 3. Calculation of Space Velocity Components and Orbital Parameters

In this section, we describe determinations of the space velocity components and orbital parameters of our SDSS/LAMOST data set.

For these computations, we adopted the distances and radial velocities of the SDSS/LAMOST sample, corrected as described above. Proper motions were adopted from Gaia EDR3. Note that we used the Gaia parallax distance for some of our program stars for which the relative error in the parallax is less than 10%, instead of their photometric distance.

The velocity components,  $V_r$ ,  $V_\theta$ , and  $V_\phi$ , are obtained in a spherical coordinate system around the Galactic center. We also obtained orbital parameters such as the apogalactic distance,  $r_{\text{apo}}$ , perigalactic distance,  $r_{\text{peri}}$ , stellar orbital

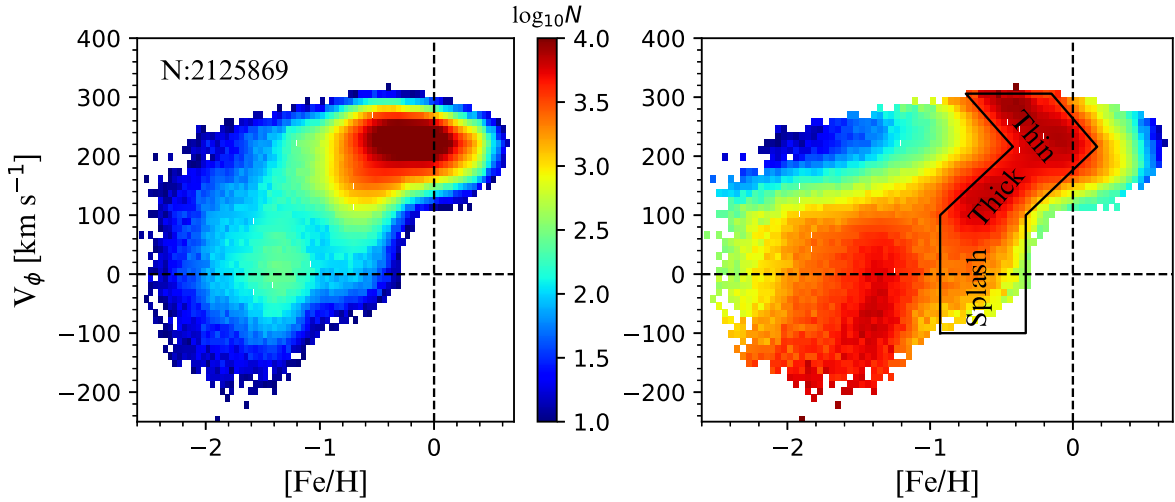


**Figure 1.** Distribution of our sample of MS/MSTO stars from SDSS and LAMOST in the  $V_\phi$ -[Fe/H] plane. Left panel: logarithmic number density. The stars in the  $V_\phi$  range of 100–300 km s<sup>-1</sup> and [Fe/H] > -1.0 mostly comprise thick- and thin-disk stars. Right panel: row-normalized number density, which consists of normalized histograms of each bin (12 km s<sup>-1</sup>) of  $V_\phi$ . The solid black line delineates likely occupants of the thin disk, thick disk, and Splash (see the text for the derivation of the boundaries). Each bin has a size of 0.04 dex by 12 km s<sup>-1</sup> in [Fe/H] and  $V_\phi$ , respectively, and contains at least ten stars.

eccentricity,  $e = (r_{\text{apo}} - r_{\text{peri}}) / (r_{\text{apo}} + r_{\text{peri}})$ , the maximum distance,  $Z_{\text{max}}$ , above or below the Galactic plane achieved during the star’s orbit, and the angular momentum vectors, in order to calculate the orbital inclination,  $i$ . We adopted a Stäckel-type potential model (see Chiba & Beers 2000; Kim et al. 2019 for details), a circular velocity of the local standard of rest  $V_{\text{LSR}} = 236 \pm 3$  km s<sup>-1</sup> (Kawata et al. 2019), the solar position of  $R_\odot = 8.2 \pm 0.1$  kpc (Bland-Hawthorn & Gerhard 2016) and  $Z_\odot = 20.8$  pc (Bennett & Bovy 2019), and solar peculiar motion  $(U, V, W)_\odot = (-11.10, 12.24, 7.25)$  km s<sup>-1</sup> (Schönrich et al. 2010).

As we are interested in exploring the chemodynamical characteristics of the Splash stars, we restricted our sample of stars to have a vertical distance of  $|Z| < 3$  kpc from the Galactic midplane, where the Splash stars are dominant. To minimize contamination from the Galactic bulge, we also imposed a projected distance of  $R > 5$  kpc onto the Galactic plane. In addition, only the stars with ruwe (renormalized unit weight error, a measure of the quality of the astrometric solution) < 1.4 from Gaia EDR3 were included in our sample. A series of these cuts resulted in a total number of 2, 125, 869 MS and MSTO stars in our sample.

#### 4. Selection of Low- $[\alpha/\text{Fe}]$ and High- $[\alpha/\text{Fe}]$ Populations

In this section, we describe how we isolate the Splash stars in the rotation velocity ( $V_\phi$ ) and metallicity ([Fe/H]) plane, and separate them into a low- $[\alpha/\text{Fe}]$  population (LAP) and a high- $[\alpha/\text{Fe}]$  population (HAP) by examining their kinematic and chemical properties, respectively.

##### 4.1. The Splash Stars

Figure 1 shows the distribution of our sample stars in the  $V_\phi$ -[Fe/H] plane. The left panel shows the logarithmic number density, while the right panel displays a row-normalized number density, which explicitly renders the correlation between  $V_\phi$  and [Fe/H]. In both panels, each bin has a size of 0.04 dex by 12 km s<sup>-1</sup> in [Fe/H] and  $V_\phi$ , respectively, and contains at least ten stars. In the left panel, the stars in the ranges  $V_\phi = +100$ – $+300$  km s<sup>-1</sup> and [Fe/H] > -1.0 are considered thin- and thick-disk stars. One interesting aspect

of the panel is that the objects in the ranges of  $V_\phi = -100$ – $+100$  km s<sup>-1</sup> and  $-2.0 < [\text{Fe}/\text{H}] < -0.3$  apparently exhibit two separate components: one at [Fe/H]  $\sim -1.5$ , which corresponds to the GSE structure (Belokurov et al. 2018; Deason et al. 2018; Kwang Kim et al. 2021), and the other at [Fe/H]  $\sim -0.7$ , which corresponds to the Splash stars (Belokurov et al. 2020).

In the right panel, inspired by Belokurov et al. (2020) but following a slightly different approach, we have separated out the thin disk, the thick disk, and the Splash, demarcated within the solid black line. To derive this region, we first divided the rotation velocity into eight sections, independent of [Fe/H], and in each section we constructed the metallicity distribution function (MDF). We then fit a Gaussian function to the constructed MDF in each section and identified the peak metallicity,  $[\text{Fe}/\text{H}]_{\text{peak}}$ , of the Gaussian function, thus obtaining eight  $[\text{Fe}/\text{H}]_{\text{peak}}$  values. Finally, we applied  $[\text{Fe}/\text{H}]_{\text{peak}} \pm 0.3$  dex to define the areas of the thin disk, the thick disk, and Splash. Note that, as the MDF for the section of  $V_\phi \sim 220$  km s<sup>-1</sup> was not well-reproduced by a Gaussian function, we used a maximum value of the MDF instead of the Gaussian peak.

Regarding the Splash region, as Belokurov et al. (2020) stated, it is not necessary to restrict the metallicity region of the Splash to that which they used ( $-0.7 < [\text{Fe}/\text{H}] < -0.2$ ). Indeed, close inspection of Figure 1 indicates that the stellar number density drops between GSE (at [Fe/H] = -1.5) and the Splash at [Fe/H]  $\sim -1.0$  for  $V_\phi < 100$  km s<sup>-1</sup>. Therefore, we defined the Splash region in this study as the area encompassed by  $-1.0 < [\text{Fe}/\text{H}] < -0.3$  and  $-100 < V_\phi < +100$  km s<sup>-1</sup>, which is slightly wider in [Fe/H] than  $[\text{Fe}/\text{H}]_{\text{peak}} \pm 0.3$  dex, and the range originally used by Belokurov et al. (2020). This metallicity range allows us to more closely scrutinize the intersection between GSE and the Splash.

Figure 2 shows the mean  $[\alpha/\text{Fe}]$  value (left) and velocity dispersion of the radial component in a spherical coordinate system in the  $V_\phi$ -[Fe/H] plane. The solid black line represents the thin-disk, thick-disk, and Splash components, as in Figure 1. From inspection, a few important features emerge in this figure. The metal-poor portion ( $[\text{Fe}/\text{H}] \lesssim -0.6$ ) in the Splash region exhibits a relatively lower mean  $[\alpha/\text{Fe}]$  and higher velocity dispersion than the metal-rich counterpart. The

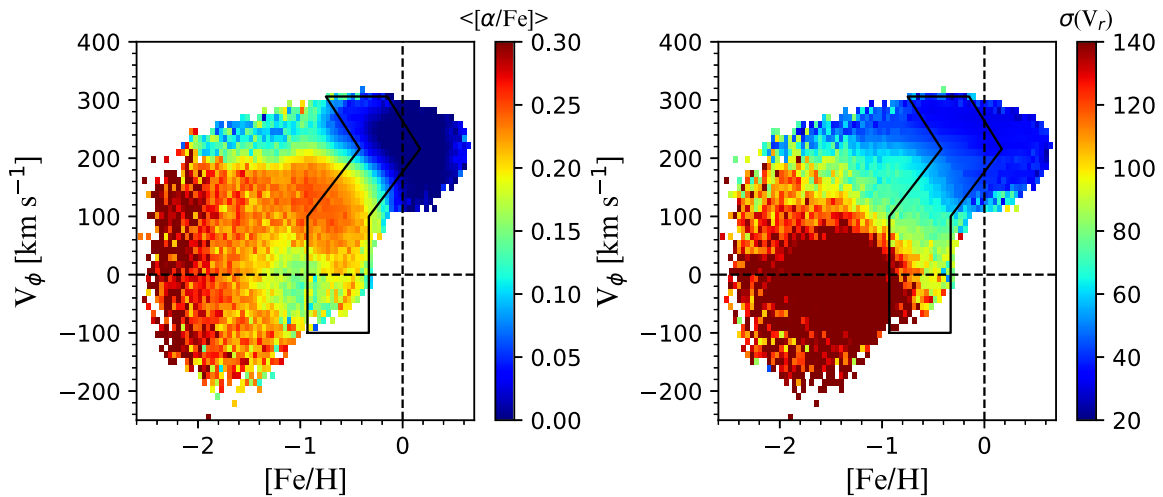


**Figure 2.** Same as in Figure 1, but for the mean  $[\alpha/\text{Fe}]$  (left) and radial velocity ( $V_r$ ) dispersion (right) in each bin. The left panel indicates that the mean  $[\alpha/\text{Fe}]$  of metal-rich ( $[\text{Fe}/\text{H}] \gtrsim -0.6$ ) stars is larger than that of the metal-poor ( $[\text{Fe}/\text{H}] \lesssim -0.6$ ) stars in the Splash region. In addition, a higher  $V_\phi$  corresponds to a larger  $[\alpha/\text{Fe}]$ . It is also clear to see in the right panel that the radial velocity dispersion of metal-rich stars is lower than that of metal-poor stars in the Splash region.

mean  $[\alpha/\text{Fe}]$  generally increases and  $\sigma(V_r)$  decreases with increasing  $V_\phi$ . The behavior of the high  $\langle[\alpha/\text{Fe}]\rangle$  and small velocity dispersion for the metal-rich stars ( $[\text{Fe}/\text{H}] \gtrsim -0.6$ ) in the Splash region indicates a smooth transition to the thick disk. However, we note that the thick-disk population exhibits a much lower velocity dispersion, hinting that the high- $[\alpha/\text{Fe}]$  stars in the Splash region may be a component of the old MW’s disk, heated by a GSE (or other) merger as reported by previous studies (Bonaca et al. 2017; Haywood et al. 2018; Gallart et al. 2019; Di Matteo et al. 2019; Belokurov et al. 2020).

One more remarkable feature in the left panel of Figure 2 is the area with relatively low  $[\alpha/\text{Fe}]$  at  $[\text{Fe}/\text{H}] \sim -1.0$  and  $V_\phi \sim 0.0 \text{ km s}^{-1}$ , which appears to be an  $\alpha$ -poor “hole,” but with high  $\sigma(V_r)$ , comparable to the GSE stars. This feature has not been recognized in the work of Belokurov et al. (2018) (see their Figure 2), and definitely deserves to be further investigated in future studies.

In summary, in the Splash region, metal-poor stars have low  $\langle[\alpha/\text{Fe}]\rangle$  and large velocity dispersions, while the metal-rich stars have high  $\langle[\alpha/\text{Fe}]\rangle$  and small velocity dispersions. These characteristics suggest that the Splash stars may comprise not only a heated component but also perhaps a new component yet to be identified. However, we recognize that, because the metal-poor part of the Splash region is the metal-rich tail of the GSE, there must be some accreted stars from the GSE as well. Furthermore, Figure 2 potentially signals that we could divide the Splash stars into LAP and HAP, based on  $\sigma(V_r)$  and  $[\alpha/\text{Fe}]$  as a function of  $[\text{Fe}/\text{H}]$ .

Before we can classify the Splash stars into LAP and HAP, we need to select likely members of the Splash stars by imposing an additional constraint on top of the defined Splash region in Figure 1. We suspect that the Splash is associated with the GSE merger event, and the Splash stars have eccentricity ( $e$ ) higher than 0.5 (Belokurov et al. 2020). In our study, we imposed a rather higher cut of  $e > 0.7$  to our sample in order to remove extreme thick-disk contamination and isolate likely Splash members, resulting in the total number of 11,562 Splash stars. Figure 3 shows the spatial distribution in the Galactic coordinate system of the selected Splash stars on a logarithmic number density scale. The figure indicates that a large fraction of our Splash stars dominate in the high Galactic latitude region, but are not found around the Galactic center

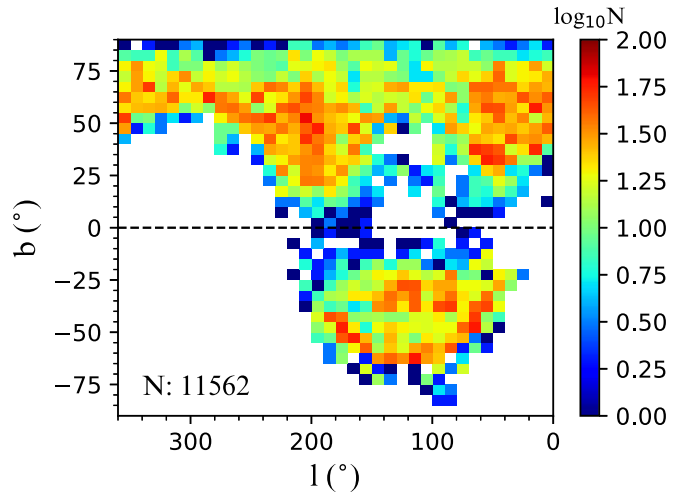


**Figure 3.** Spatial distribution in the Galactic coordinate system of selected Splash stars on a logarithmic density scale, as indicated in the color bar at the right.

and disk regions due to high reddening. We also see a large portion of the stars in the anticenter direction, most of which come from LAMOST. Because the SDSS and LAMOST were carried out in the Northern Hemisphere, a greater fraction of the stars are in the northern part of the MW galaxy.

#### 4.2. Division of the LAP and HAP Populations

Figure 4 shows the radial velocity dispersion (left panel) and the logarithmic number density (right panel) of the selected Splash stars in the  $[\alpha/\text{Fe}]$ – $[\text{Fe}/\text{H}]$  space. Each bin has a size of 0.05 by 0.03 dex in  $[\text{Fe}/\text{H}]$  and  $[\alpha/\text{Fe}]$ , respectively, and contains at least five stars. We applied a Gaussian kernel to the original distribution in order to obtain a smooth distribution. It is apparent from the left panel that the Splash stars are separable into two groups of stars: one with a large  $V_r$  dispersion and the other with a small  $V_r$  dispersion. It is also obvious that the stars with large  $\sigma(V_r)$  mostly exhibit low  $[\alpha/\text{Fe}]$ , while the ones with small  $\sigma(V_r)$  dispersions are mostly dominant at high  $[\alpha/\text{Fe}]$ , at a given  $[\text{Fe}/\text{H}]$ . To quantify the

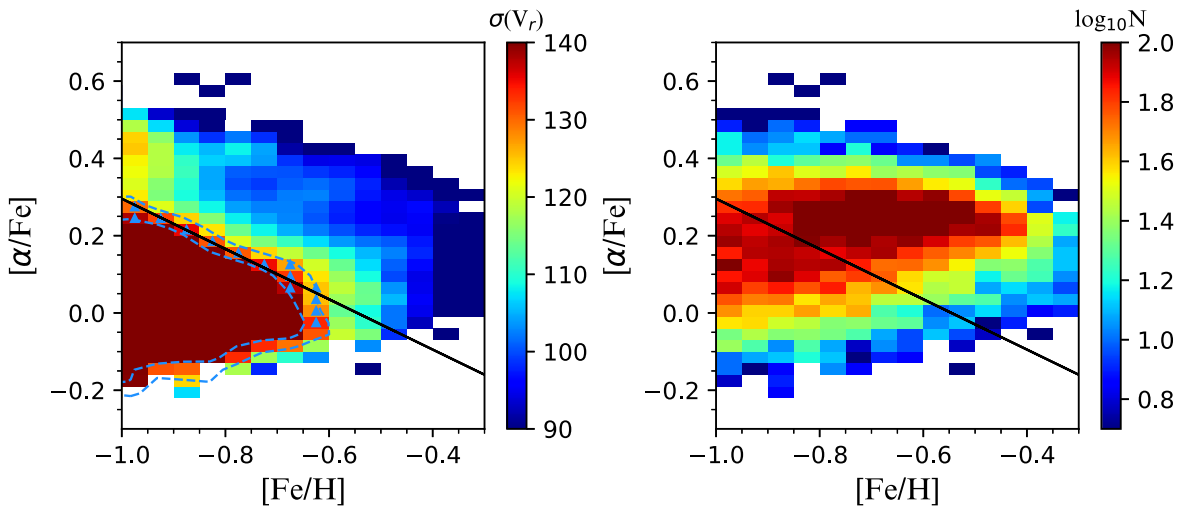


**Figure 4.** Distribution of selected Splash stars in the  $[\alpha/\text{Fe}]$ - $[\text{Fe}/\text{H}]$  plane. Left panel: distribution of the radial velocity ( $V_r$ ) dispersion. The blue contours indicate the radial velocity dispersions at  $125 \text{ km s}^{-1}$  and  $140 \text{ km s}^{-1}$ , respectively. Blue triangles show the positions of bins between the two blue contours for  $[\alpha/\text{Fe}] > -0.05$ . The black solid line follows  $[\alpha/\text{Fe}] = -0.35 - 0.65 \times [\text{Fe}/\text{H}]$ . We define the stars above this line as the high- $[\alpha/\text{Fe}]$  population (HAP) and the stars below it as the low- $[\alpha/\text{Fe}]$  population (LAP). Right panel: logarithmic number density distribution, with the same solid black line as in the left panel. In both panels, each bin has a size of 0.05 dex by 0.03 dex in  $[\text{Fe}/\text{H}]$  and  $[\alpha/\text{Fe}]$ , respectively, and contains at least five stars.

apparent dichotomy, we derived a boundary line, as a function of  $[\text{Fe}/\text{H}]$ , to divide the two groups of stars as described below.

First, we examined contours in the  $\sigma(V_r)$  map. Then, by choosing two contours (blue contours in the left panel of Figure 4) of  $125 \text{ km s}^{-1}$  and  $140 \text{ km s}^{-1}$  as boundaries, we identified in the  $[\alpha/\text{Fe}]$ - $[\text{Fe}/\text{H}]$  plane the positions (blue triangles) of bins between the two blue contours for  $[\alpha/\text{Fe}] > -0.05$ . We then performed a least-squares fit with  $2\sigma$  clipping to the positions (blue triangles) to obtain a linear relationship of  $[\alpha/\text{Fe}] = -0.35 - 0.65 \times [\text{Fe}/\text{H}]$  (black solid line in Figure 4). The stars above the line are defined as the HAP, and the stars below the line are considered the LAP. Even though we used  $[\alpha/\text{Fe}]$  and  $[\text{Fe}/\text{H}]$  for the division, as we followed the velocity dispersion in the chemical frame, it would be more appropriate to name each population HAP with high  $\sigma(V_r)$  and LAP with low  $\sigma(V_r)$ . But for simplicity of the nomenclature, we just refer to them as LAP and HAP for the remainder of this analysis.

The right panel of Figure 4 displays the logarithm of the stellar number density, with the adopted dividing line marked as the black solid line. The small radial velocity dispersion region in the left panel is apparently the highest-density region at  $[\alpha/\text{Fe}] \sim +0.2$  in the right panel.

In order to check if there is any spatial bias between the selected LAP and HAP, we examined the spatial distribution of the LAP and HAP on a logarithmic number density scale in the Galactocentric Cartesian reference frame, as shown in Figure 5. The axes  $X$ ,  $Y$ , and  $Z$  are positive in orientation toward the Sun, Galactic rotation, and north Galactic pole, respectively. Each bin has a size of 0.2 kpc by 0.1 kpc in the abscissa and ordinate, respectively. The figure indicates that, even though both populations have different numbers of stars, they exhibit similar spatial distribution, indicating no significant bias in the spatial distribution. We also observe that most of our program stars are located around the solar circle between 6 and 11 kpc from the Galactic center.

## 5. Results

In this section, we search for any distinct features in the LAP and HAP populations that may provide clues to their origin.

### 5.1. Kinematic Property of LAP and HAP

To check if the two populations identified in Figure 4 show any contrast (similarity) from (to) the canonical thin disk and thick disk, we compared the profiles of  $\sigma(V_r)$ , as functions of  $[\alpha/\text{Fe}]$  (left) and  $[\text{Fe}/\text{H}]$  (right), for the LAP, HAP, thin disk, and thick disk, as shown in Figure 6. The red circles, black crosses, green triangles, and blue down triangles represent the LAP, HAP, thick, and thin disk, respectively. We also show the  $\sigma(V_r)$  profile (cyan) of our selected Splash stars. The thin- and thick-disk populations were selected using the method of Han et al. (2020), which is mainly based on the level of  $\alpha$ -enhancement with respect to  $[\text{Fe}/\text{H}]$ , along with some spatial and kinematic constraints. The  $\sigma(V_r)$  value of the LAP, HAP, and Splash stars was calculated with bins of 600 stars, while the thin-disk and thick-disk values were calculated with 2000 stars per bin. We took a median value for  $[\alpha/\text{Fe}]$  and  $[\text{Fe}/\text{H}]$  for each bin. The velocity dispersion gradient of each population in the right panel was obtained through a least-squares fit to the data points; it is listed in the upper right legend. The very small gray symbol is the error bar, which was derived by bootstrapping each bin sample 1000 times.

One intriguing aspect of the  $\sigma(V_r)$  profiles in the left panel of Figure 6 is the abrupt change in the range  $[\alpha/\text{Fe}] = +0.1$ – $+0.2$  for the Splash stars (cyan). The change in  $\sigma(V_r)$  amounts to about  $40 \text{ km s}^{-1}$ , suggesting that more than one physical process may be responsible for the formation of the Splash stars. Additionally, we note that the  $\sigma(V_r)$  profiles of the LAP and HAP samples do not change much with  $[\alpha/\text{Fe}]$ . The diversity in the kinematics of the Splash stars also validates our approach of separating them into two groups in this figure.

The right panel of Figure 6 obviously exhibits different means and gradients of  $\sigma(V_r)$  with respect to  $[\text{Fe}/\text{H}]$  in each population. As is well-known (e.g., Lee et al. 2011b; Han et al. 2020), the thick-disk component has a larger mean and steeper gradient than those of the thin-disk component. The  $\sigma(V_r)$  mean and slope of the LAP are larger and steeper than for the HAP, and the mean and gradient of  $\sigma(V_r)$  for both populations are higher and steeper than those of the canonical disks. These characteristics were also reported by Belokurov et al. (2020).

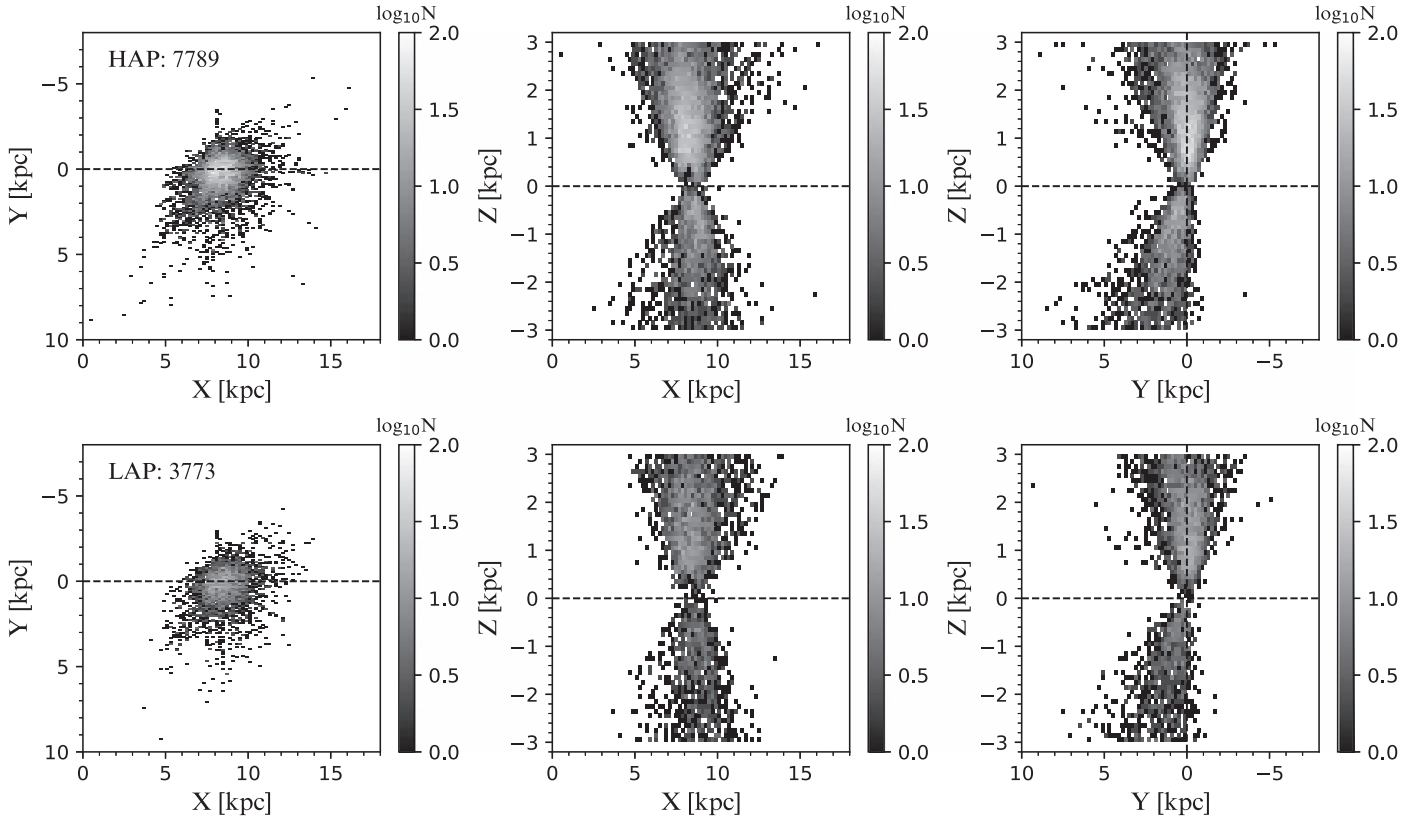


**Figure 5.** Spatial distribution of selected LAP (top) and HAP (bottom) on a logarithmic scale. A Galactocentric Cartesian reference frame is used. Each bin has a size of 0.2 kpc by 0.1 kpc in X-axis and Y-axis, respectively. We see that most of the stars are located within 6–11 kpc from the Galactic center.

By comparison, we obtained a mean value of  $\sigma(V_r)$  of  $108.0 \pm 1.0 \text{ km s}^{-1}$  for the HAP, which is in excellent agreement with that ( $108 \pm 19 \text{ km s}^{-1}$ ) of the Splash stars defined in Belokurov et al. (2020), while the average  $\sigma(V_r)$  of the LAP (assuming that all stars in the LAP are accreted from the GSE) is  $160.0 \pm 2.0 \text{ km s}^{-1}$ , which is slightly lower than the  $175 \pm 26 \text{ km s}^{-1}$  from Belokurov et al. (2020).

One remarkable feature noticeable in the right panel of Figure 6 is that the slope of the HAP is similar to the thick-disk population, within error bars, although the magnitude of average  $\sigma(V_r)$  differs by about  $46.0 \pm 1.0 \text{ km s}^{-1}$ , which is close to the difference of  $35 \text{ km s}^{-1}$  found by Belokurov et al. (2020). As envisaged in numerous previous studies (e.g., Di Matteo et al. 2019; Gallart et al. 2019; Mackereth et al. 2019; Belokurov et al. 2020), this kind of kinematic connection between these populations can arise from the dynamical heating of the primordial disk by the GSE merger. Independent of metallicity, the old disk stars could have been collectively perturbed by the GSE to higher velocity dispersions, while keeping their  $\sigma(V_r)$  slope over  $[\text{Fe}/\text{H}]$  unchanged, and the heated stars could have become the current HAP.

Although, due to the small number of data points for the LAP compared to other populations, the uncertainty of the  $\sigma(V_r)$  gradient of the LAP is rather large, we clearly observe, on average, a much higher  $\sigma(V_r)$ , which is kinematic evidence for its distinct properties. We carried out a two-sample Kolmogorov–Smirnov (KS) test between the LAP and HAP for the orbital parameters  $Z_{\text{max}}$  and  $r_{\text{apo}}$  to check if the two populations share a common origin. We obtained a  $p$  value much less than 0.01, and thus we can reject the null hypothesis that the two components share the same parent population.

## 5.2. Chemical Properties of the LAP and HAP

Here, we consider the chemical nature of the LAP, HAP, and canonical disks in order to identify any possible contrast in chemistry among them. For this exercise, we included the GSE stars. The results of this investigation are shown in Figure 7, which plots the mean  $[\text{Mg}/\text{Fe}]$  profiles as a function of  $[\text{Fe}/\text{H}]$ . The symbols are the same as in the right panel of Figure 6, except for the magenta symbols of the GSE stars, which were selected by simple cuts of  $[\text{Fe}/\text{H}] < -0.7$  and eccentricity  $> 0.7$ , after excluding the HAP. Each bin of the LAP and HAP has a size of 0.1 dex, but that of the GSE stars has a size of 0.3 dex. For the thick disk and the thin disk, we used a bin size of 0.2 dex to obtain the mean abundances. For each population, if the number of stars in each bin is less than 100, we used a larger bin size to increase the number of stars up to 100. For this reason, the leftmost and rightmost bins are larger. The gray shaded area in Figure 7 is the Splash region we defined.

One notable feature in Figure 7 is that the HAP and thick-disk stars exhibit very similar decreasing trends of  $[\text{Mg}/\text{Fe}]$  profiles with increasing  $[\text{Fe}/\text{H}]$  in the Splash region. The LAP presents a relatively lower  $[\text{Mg}/\text{Fe}]$  profile than that of the HAP, as expected, due to their chemical separation. The  $[\text{Mg}/\text{Fe}]$  profile of the GSE indicates that the so-called  $\alpha$ -knee occurs at  $[\text{Fe}/\text{H}] \sim -1.2$ , lower than that of the Galactic disk system, which agrees with that ( $[\text{Fe}/\text{H}] = -1.3$ ) obtained by other studies (Belokurov et al. 2018; Helmi et al. 2018; Mackereth et al. 2019). We also observe that its profile falls on that of the LAP within the estimated errors, which implies that the metal-poor region ( $[\text{Fe}/\text{H}] < -0.7$ ) of the LAP may include some portion of the accreted stars from the GSE event (Belokurov et al. 2018; Helmi et al. 2018).

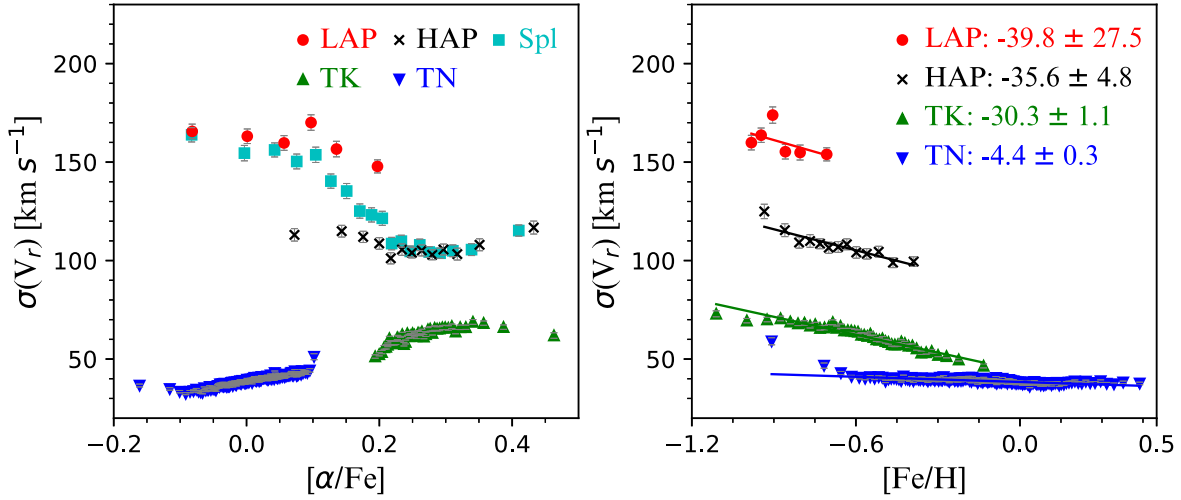


**Figure 6.** Profiles of  $\sigma(V_r)$ , as functions of  $[\alpha/\text{Fe}]$  (left panel) and  $[\text{Fe}/\text{H}]$  (right panel), for selected groups of stars: red circles for the LAP, black crosses for the HAP, green triangles for the thick disk (TK), and blue downward triangles for the thin disk (TN). The cyan squares in the left panel represent our selected Splash stars. The  $\sigma(V_r)$  value for the red circles, black crosses, and cyan squares was computed from 600 stars in each bin, while the one for the green triangles and downward blue triangles includes 2000 stars per bin. The very small error bar in gray was obtained from 1000 bootstrapped samples. We took a median value for  $[\alpha/\text{Fe}]$  and  $[\text{Fe}/\text{H}]$  for each datum. The slope of  $\sigma(V_r)$ , as a function of  $[\text{Fe}/\text{H}]$ , shown in the right panel was derived by a least-squares fit to the binned data.

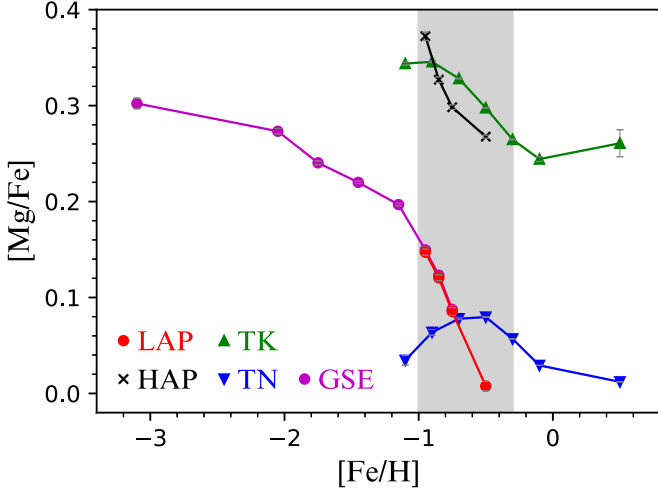


**Figure 7.** Mean profiles of  $[\text{Mg}/\text{Fe}]$ , as a function of  $[\text{Fe}/\text{H}]$ . The symbols are the same as in the right panel of Figure 6, except for the magenta color, which represents the GSE stars (see text for the selection of the stars). We calculated the mean of respective abundance ratio value in each bin of  $[\text{Fe}/\text{H}]$ . Each bin of the HAP and LAP has a size of 0.1 dex, but for the GSE stars, we used a bin size of 0.3 dex. For the thick disk and thin disk, we determined the average value of each abundance ratio in a bin size of 0.2 dex. Note that, because we forced each bin to contain at least 100 stars, the leftmost or rightmost bin size is larger in each profile. The gray shaded region indicates the Splash.

It is also interesting to note that the LAP's  $[\text{Mg}/\text{Fe}]$  profile overlaps with and becomes lower than that of the thin disk, indicating that the metal-rich end of the LAP did not undergo star formation as quickly and intensively as the Galactic thin disk, but was chemically enriched by more supernovae of Type Ia (SNe Ia).

## 6. Discussion

In Section 5, we have demonstrated that the Splash does not comprise a single population, because the chemodynamically separated LAP and HAP of the Splash stars exhibit different chemistry and kinematics in several aspects. It appears that

their diverse chemodynamical characteristics are associated with the GSE merger event.

According to various hydrodynamical simulations (e.g., Gallart et al. 2019; Belokurov et al. 2020; Grand et al. 2020), the two major effects of the GSE merger on the Galactic disk are the dynamical heating of the proto-disk of the MW and the trigger of star formation during the GSE event. In this section, we take a closer look into the dynamical properties of the LAP and HAP, and we discuss their origin by considering these two major effects from the GSE.

In Figures 6 and 7, we observed that the  $\sigma(V_r)$  gradient of the HAP is very close to that of the thick-disk population, with a mean  $\sigma(V_r)$  much larger than that of the thick disk, and the HAP exhibits a level of  $[\text{Mg}/\text{Fe}]$  similar to that of the canonical thick disk, as reported by several previous studies (Nissen & Schuster 2010; Hawkins et al. 2015; Bonaca et al. 2017; Haywood et al. 2018; Di Matteo et al. 2019; Belokurov et al. 2020).

However, we have found rather different aspects for the LAP in Figures 6 and 7. The LAP possesses even larger  $\sigma(V_r)$  with a steeper gradient (albeit with a relatively large error bar) than the thick disk. Chemically, the  $[\text{Mg}/\text{Fe}]$  trend of the LAP declines steeply, and their  $[\text{Mg}/\text{Fe}]$  becomes lower than that of the thin disk (blue downward triangles in Figure 7) at  $[\text{Fe}/\text{H}] > -0.7$ .

It is believed that the high- $[\alpha/\text{Fe}]$  thick disk first was established before 8–10 Gyr ago, and later on the thin disk has built up its mass gradually. Consequently, we can naturally reason that the HAP could arise from the dynamical heating of the primordial disk with high- $[\alpha/\text{Fe}]$  by the GSE merger, because the occurrence of the GSE event is predicted to have taken place around 8–11 Gyr ago (Belokurov et al. 2018; Mackereth et al. 2019). We can imagine that the stars in the pre-existing disk were collectively perturbed by the GSE merger, altering their orbits and achieving higher velocity dispersion. However, the already established  $\sigma(V_r)$  gradient over  $[\text{Fe}/\text{H}]$  would be preserved, again as revealed by other studies (e.g., Bonaca et al. 2017; Haywood et al. 2018; Di Matteo et al. 2019; Belokurov et al. 2020).



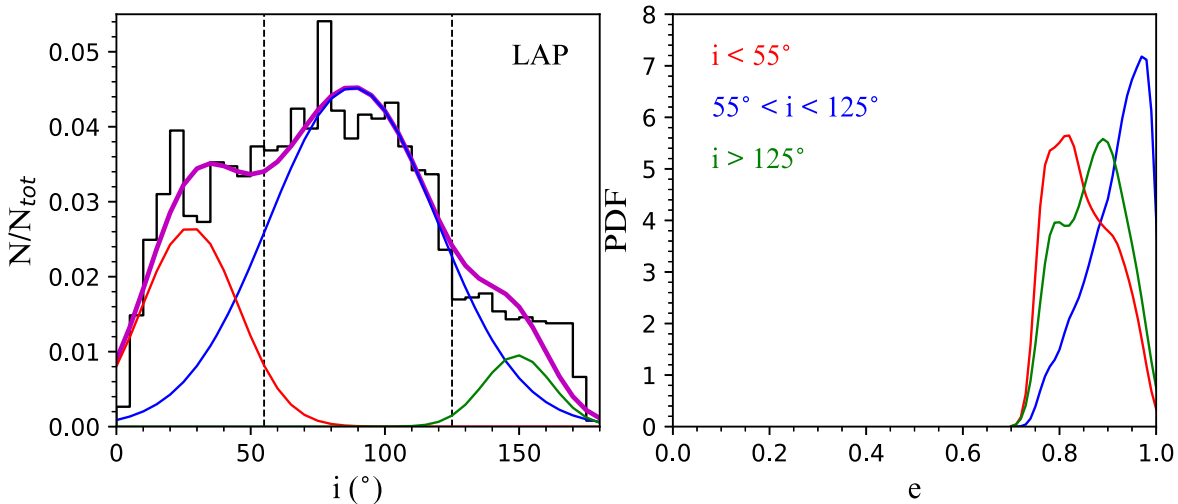


**Figure 8.** Left panel: distribution of the orbital inclinations ( $i$ ) of the LAP. The black histogram comes from the LAP, while the magenta solid line represents the sum of three Gaussian components (red, blue, and green curves). The two vertical dashed lines mark  $i = 55^\circ$  and  $i = 125^\circ$ , respectively. Right panel: Kernel density estimation of the eccentricity ( $e$ ) distribution of the LAP. The blue solid line is for stars with high inclination  $55^\circ < i < 125^\circ$ , the red solid line for  $i < 55^\circ$ , and the green solid line is for  $i > 125^\circ$ . Note that the stars with  $i > 90^\circ$  are counter-rotating.

If the GSE merger occurred about 10 Gyr ago (Belokurov et al. 2018; Helmi et al. 2018; Mackereth et al. 2019), and the thin disk formed since then, chronologically, it is difficult to imagine that the LAP once belonged to the thin disk and was heated up to achieve halo-like kinematics during the GSE merger event. Moreover, its  $[\alpha/\text{Fe}]$  (at  $[\text{Fe}/\text{H}] > -1.0$ ) is too low to consider to be a heated population from the primordial disk. Consequently, it is more natural to think that the LAP was accreted from the GSE or formed out of the chemically evolved gas brought by a merger event such as the GSE. Whether or not the LAP was accreted or formed in situ, because the progenitor (s) of the GSE had a very elongated orbit (Belokurov et al. 2018; Helmi et al. 2018; Mackereth et al. 2019), we might expect to observe high  $\sigma(V_t)$  in the LAP. This interpretation agrees to some degree with the predictions by hydrodynamical simulations (e.g., Belokurov et al. 2020; Grand et al. 2020; Dillamore et al. 2022).

However, there are other interpretations for the formation of the Splash stars. For example, Amarante et al. (2020) claimed, based on a hydrodynamical simulation of an isolated galaxy producing clumps of star formation, that the Splash stars (with high metallicity,  $[\text{Fe}/\text{H}] > -1.0$ , and low rotation velocities), including retrograde stars, could be formed via scattering off of such clumps, without the need for a major merger such as the GSE.

Zhao & Chen (2021) have presented an argument similar to the above. Using a LAMOST sample of giants, they attempted to explain the origin of so-called metal-rich Sausage-kinematic (MRSK) stars, which correspond to the Splash stars. Because the low- and high- $[\alpha/\text{Fe}]$  stars among their MRSK stars exhibit similar characteristics in the dynamical space, they argued that those stars originated from the same physical process. They further claimed that the process that produced the Splash is not responsible for the presence of the low- $[\alpha/\text{Fe}]$  stars, because using  $[\alpha/\text{Fe}]$  as an age proxy, the low  $[\alpha/\text{Fe}]$  implies a young age, which cannot be reconciled with the epoch of the GSE merger event. Having claimed that the low- $[\alpha/\text{Fe}]$  stars may not have been produced by dynamical heating of the proto-disk by the GSE, they followed the suggestion of Amarante et al. (2020) that gas-rich clumps that were developed during the

GSE merger produced the bimodal distribution in  $[\alpha/\text{Fe}]$ , as seen their MRSK stars.

Nonetheless, motivated by the fact that, in our MS/MSTO sample, there is no analogy to the kinematic structures between the LAP and the HAP, we have considered a more detailed dissection of the LAP in dynamical space, and found some interesting characteristics. The left panel of Figure 8 shows the distribution of the orbital inclination ( $i$ ) of the LAP. This panel reveals that a Gaussian decomposition to the observed distribution (black histogram) requires at least three components, represented by one blue distribution of high orbital inclination ( $55^\circ < i < 125^\circ$ ), one red distribution of low orbital inclination ( $i < 55^\circ$ ), and one green distribution of low orbital inclination ( $i > 125^\circ$ ), indicative of three distinct populations. Note that the stars with  $i > 90^\circ$  possess retrograde motions around the Galactic center; hence, stars with  $i$  close to  $180^\circ$  have low inclination and retrograde motion. We followed the same scheme used by Kwang Kim et al. (2021) for the inclination separation.

We next examined the orbital eccentricity distribution of the three groups, as shown in the right panel of Figure 8. Inspection of this panel reveals that, while the prograde, low- $i$  stars (red) are distinguishable from the high- $i$  stars (blue), their distribution overlaps a large fraction of the retrograde, low- $i$  stars (green), even though their peaks slightly differ, implying that they might be associated with each other.

It is known that stars with extreme eccentricities ( $e > 0.9$ ) in the solar neighborhood are mostly accreted from the GSE (Belokurov et al. 2018; Deason et al. 2018). Considering their low  $[\alpha/\text{Fe}]$  and high eccentricity (mostly  $e > 0.85$ ), we speculate that the high- $i$  stars are probably accreted from the GSE. On the other hand, the low- $i$  prograde and retrograde stars require a different physical process to explain their existence, such as a star formation induced by a merger event. It is known that the starburst by the GSE can produce eccentric counter-rotating stars (albeit a relatively small fraction in our case) as well as a compact disk-like component (e.g., Grand et al. 2020), which presumably has relatively low inclination. Belokurov et al. (2020) also showed in their simulations that, due to the infall of gas, gas-rich mergers at an early epoch can

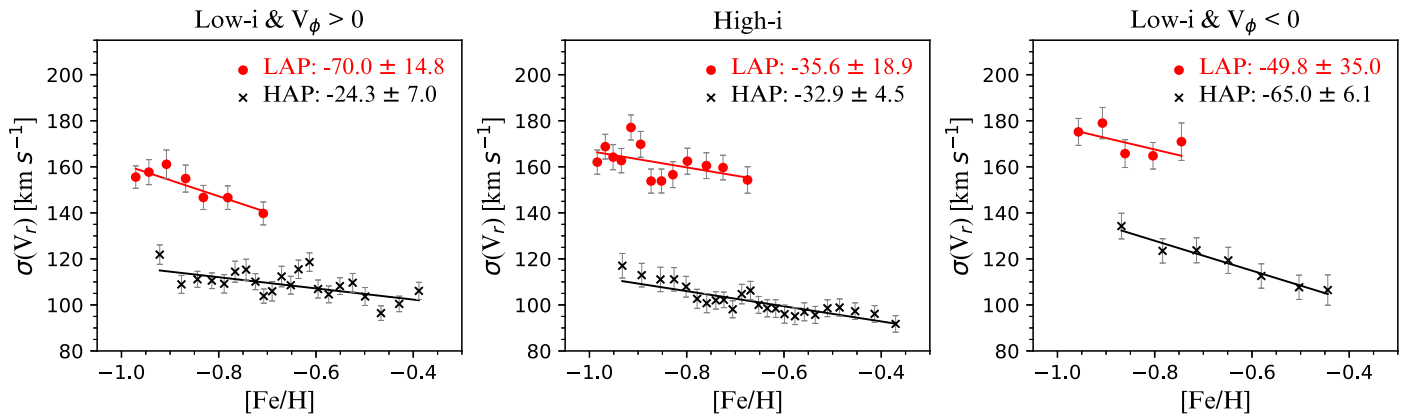


**Figure 9.** Profiles of radial velocity dispersion, as a function of  $[\text{Fe}/\text{H}]$ , for three groups of stars separated by orbital inclination ( $i$ ) and rotation velocity ( $V_\phi$ ). The definitions of low and high  $i$  are the same as in Figure 8. The red circle represents the LAP, and the black cross represents the HAP. The  $\sigma(V_r)$  value is computed from bins of 300, 300, and 200 stars with 150, 150, and 100 objects overlapped with the next neighboring bin for the left, middle, and right panel, respectively. For each bin in metallicity, we took an average of  $[\text{Fe}/\text{H}]$ . The derived gradient of  $\sigma(V_r)$  and its associated error for each group are listed in the upper right.

form another population of stars, which is distinct from the Splash.

Following the predictions by the numerical simulations, our low- $i$  stars can be regarded as the stellar population that arose from gas chemically enriched by the GSE, recalling the Galactic Starburst Sequence (GSS) discovered in An et al. (2023). They carried out a chemo-kinematical analysis of Galactic stars using photometric survey data from SDSS, the SkyMapper Sky Survey (Onken et al. 2019), and the Pan-STARRS1 surveys (Chambers et al. 2016), as well as Gaia parallaxes and proper motions, and identified the GSS, the coherent stellar structure in the high-proper-motion sample. They concluded, based on the scale-length and scale-height distributions, that some of the Splash stars formed during this starburst episode. Interestingly, our result also points out that the LAP consists of at least two distinct groups of stars.

Another observational hint that there are two distinct components of the LAP is provided in Figure 9, which plots the  $\sigma(V_r)$  gradient, as a function of  $[\text{Fe}/\text{H}]$ , for three groups of stars in the LAP (red) and the HAP (black). The definition of the three groups of stars is the same as in Figure 8: high- $i$ , low- $i$  and prograde motion ( $V_\phi > 0 \text{ km s}^{-1}$ ), and low- $i$  and retrograde motion ( $V_\phi < 0 \text{ km s}^{-1}$ ). In the figure, we can clearly see for the LAP that the  $\sigma(V_r)$  slope of low- $i$ , prograde stars is smaller than that of high- $i$  stars. The low- $i$ , retrograde group has a similar behavior, even though it is not as clear as that of the low- $i$ , prograde group, due to the relatively large error of its slope. One may expect that the prograde and retrograde low- $i$  stars in the LAP may have a similar  $\sigma(V_r)$  gradient, if they are assumed to be formed during the starburst by the GSE. The discrepancy in the gradient may be explained by a metal-rich population among the low- $i$ , prograde stars that drives a negative gradient stronger than that of the low- $i$ , retrograde stars, although the slope of the latter has a large uncertainty in our study. Nevertheless, the trend seen in Figure 9 is another telltale sign of the presence of the two populations in the LAP. According to our interpretation of the LAP, the accreted components account for  $54\% \pm 1\%$  and  $46\% \pm 1\%$  of the in situ component.

From inspection of Figure 9, within the HAP, the  $\sigma(V_r)$  slope and the overall velocity dispersion of the prograde, low- $i$  stars are similar to those of high- $i$  stars, whereas the retrograde, low- $i$  stars exhibit features different from those of the other two, with much steeper  $\sigma(V_r)$  gradient and higher mean  $\sigma(V_r)$ . Assuming

that the HAP is a heated population of the primordial disk during the GSE merger, it is rather challenging to envision that the originally prograde, low- $i$  stars in the primordial disk drastically altered their orbits to retrograde with low  $i$  as a result of the GSE merger. It is more plausible to suspect that, as in the case of the low- $i$ , counter-rotating stars in the LAP, they are formed from the gas enriched within the GSE, as ancient gas-rich mergers are very susceptible to produce stars with ranges of  $\alpha$ -element abundances (e.g., Brook et al. 2004, 2007, 2012; Grand et al. 2018; Mackereth et al. 2018; Buck 2020). However, the merger-induced population accounts for a very small fraction (9%) in the HAP sample.

The distinct populations observed in our LAP and HAP appear in accord with the expectations of numerical simulations. Nevertheless, there are some inconsistent behaviors. According to the GSE-like merger simulation by Grand et al. (2020), the proto-disk stars and the in situ stars formed by a starburst reside in a common area in  $V_\phi$ - $[\text{Fe}/\text{H}]$  space (their Figure 8). Furthermore, their simulation indicates the establishment of a positive relation, on average, between metallicity and rotation velocity due to the merger. This is because, as the proto-disk evolves and is chemically enriched prior to the GSE merger, the older, relatively metal-poor proto-disk stars are more susceptible to being dynamically heated—owing to multiple smaller mergers—than the younger, more metal-rich stars. The starburst component is more chemically enriched and possesses more rotation relative to the primordial disk of the MW. We note, however, that because the scatter of  $V_\phi$  for the starburst population in the simulation is rather large in such a small metallicity range, compared to the heated population, its apparent correlation between  $V_\phi$  and  $[\text{Fe}/\text{H}]$  may be not that significant.

The above behavior is not obviously seen in the  $V_\phi$  behavior in our sample, as can be appreciated from Figure 10, which shows profiles of the rotation velocity,  $V_\phi$ , as a function of  $[\text{Fe}/\text{H}]$ , for the LAP (red), the HAP (black), and the Splash stars (blue), which are comprised of the LAP and HAP. The  $V_\phi$  gradient of the HAP exhibits a relatively flat gradient, unlike the prediction by the simulation of Grand et al. (2020); such a small gradient seems to arise from the relatively metal-rich ( $[\text{Fe}/\text{H}] > -0.6$ ) stars in the HAP. We also recognize that this is likely to be due to our sample selection of Splash stars, which are confined to  $e > 0.7$ , which systematically eliminates high- $V_\phi$  stars, as can be inferred from Figure 10. Nonetheless,

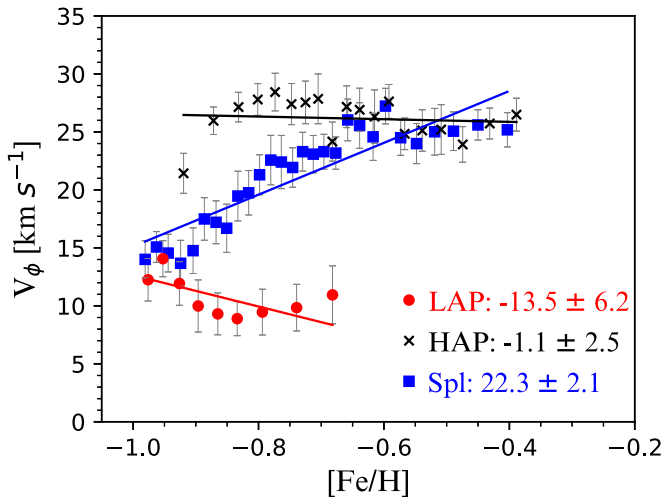


**Figure 10.** Profiles of rotation velocity,  $V_\phi$ , as a function of  $[\text{Fe}/\text{H}]$ , for selected groups of stars. The red symbols represent the LAP, the black symbols are for the HAP, and the blue are for the Splash stars, which are comprised of the LAP and HAP. Each dot is a median value of 800 stars with 400 stars overlapped with the next neighboring dot. The error bars were calculated from 1000 bootstrapped samples.

the mean  $V_\phi$  value of  $21.0 \pm 1.0 \text{ km s}^{-1}$  for the HAP agrees well with that of the Splash population ( $25 \text{ km s}^{-1}$ ) reported by Belokurov et al. (2020).

Concerning the LAP, even if we take the overall increasing trend of  $V_\phi$  as a positive gradient from the simulation, the  $V_\phi$  trend of our LAP is far from a positive. We even see a negative gradient (although we could derive a slightly positive slope of  $12.4 \pm 1.7 \text{ km s}^{-1} \text{ dex}^{-1}$  by only taking into account the points with  $[\text{Fe}/\text{H}] > -0.85$ ). If our LAP is dominated by the starburst population, we would expect a positive slope as the theory predicts, but the opposite behavior is observed in the figure.

Considering that the starburst population identified by Grand et al. (2020) is mostly located in the lower  $[\alpha/\text{Fe}]$  region, compared to the proto-disk stars, and has a metallicity range similar to that of the LAP, setting aside the existence of the positive  $V_\phi$  gradient, a possible explanation for the negative slope of the LAP is that it is more dominated by accreted stars from the GSE, rather than by stars formed by the starburst. This resolution concurs with the large fraction (54%) of high- $i$  stars in Figure 8, which are regarded as being accreted from the GSE. When combining the LAP and HAP, we find a positive  $V_\phi$  slope, as can be seen in Figure 10, which is once again a clear signature of the two distinct populations.

In Figure 7, we have seen that the  $[\text{Mg}/\text{Fe}]$  profile trend of the LAP overlaps with that of the thin disk, and it even becomes lower. Regarding this trend, it is worthwhile to mention that Myeong et al. (2022) recently reported the identification of a new stellar component, dubbed “Eos,” using giants with  $e > 0.85$  in APOGEE DR17 (Abdurro’uf et al. 2022) and GALAH DR3 (Buder et al. 2021) database. The Eos stars are mostly located in between the high- $[\alpha/\text{Fe}]$  and relatively low- $[\alpha/\text{Fe}]$  GSE stars at given metallicity in the  $[\alpha/\text{Fe}]$ - $[\text{Fe}/\text{H}]$  diagram, and they cover the metallicity range  $-1.0 < [\text{Fe}/\text{H}] < -0.3$ , which is apparently the same range as ours. They have also noticed that the chemical evolution of the Eos stars has proceeded from the GSE to the low- $[\alpha/\text{Fe}]$  thin disk, as can be seen in our LAP. They concluded that, because their  $[\text{Al}/\text{Fe}]$  level is higher than that of the GSE stars, but not as high as that of the heated population (Splash), the Eos stars

are not accreted, but instead are formed in the gas chemically enriched by the GSE. Thereby, their claim strengthens our view that the low- $[\alpha/\text{Fe}]$  Slash-like stars in our sample should consist of at least two separate populations: those accreted and those formed in situ by the starburst.

Our claim for the existence of in situ stars formed by the starburst among the Splash stars is in line with the work by An et al. (2023), which demonstrated that the Splash comprises two distinct stellar populations of stars: a dynamically heated population and the GSS triggered by the GSE merger.

## 7. Summary and Conclusions

We selected 11,562 Splash-like stars in the ranges  $-100 < V_\phi < 100 \text{ km s}^{-1}$ ,  $-1.0 < [\text{Fe}/\text{H}] < -0.3$ , and  $e > 0.7$ , using MS and MSTO stars from SDSS and LAMOST, and separated them into two groups of stars, namely the LAP and the HAP, based on kinematics and chemistry. We then searched for distinct kinematic and chemical trends among them, to explore any interconnections with the GSE, and explored their likely origin. Our findings are summarized below.

We found that the  $\sigma(V_r)$  slope ( $-35.6 \pm 4.8 \text{ km s}^{-1} \text{ dex}^{-1}$ ) with respect to  $[\text{Fe}/\text{H}]$  of the HAP is very similar to that of the thick-disk population, with its mean  $\sigma(V_r)$  being much larger than that of the thick disk, and the HAP possesses levels of  $[\text{Mg}/\text{Fe}]$  to similar those of the canonical thick disk. By further investigating the distribution of the orbital inclination of the HAP, along with the  $\sigma(V_r)$  trend with  $[\text{Fe}/\text{H}]$ , we came to the conclusion that, even though the HAP is mostly dominated by stars from the dynamically heated primordial disk, there may also be a small fraction ( $9 \pm 1\%$ ) of stars that could have formed from the starburst during the GSE merger event.

On the other hand, we have observed for the LAP that it has even larger  $\sigma(V_r)$ , with a steeper gradient than the thick disk, and the  $[\text{Mg}/\text{Fe}]$  trend of the LAP decreases steeply with increasing  $[\text{Fe}/\text{H}]$ , and then the level of  $[\text{Mg}/\text{Fe}]$  becomes lower than that of the thin disk. A more detailed analysis of the orbital inclination of the LAP allowed us to infer that the majority ( $54\% \pm 1\%$ ) of the LAP is an accreted population, but there is also some portion ( $46\% \pm 1\%$ ) of the stars that possibly formed out of the chemically enriched gas within the GSE, as various numerical simulations predict.

To sum up, it appears that the HAP arises from mainly heated stars ( $\sim 91\%$ ) and a small fraction ( $\sim 9\%$ ) of in situ stars from the GSE-induced starburst. Roughly half of the LAP is made up of (54%) stars accreted from the GSE, and the other half (46%) are stars formed by the GSE starburst. These results can, of course, be changed, depending on how the Splash, LAP, and HAP stars are selected.

Regardless of the specific details, the large fraction of metal-rich, high-eccentricity, halo-like stars with low angular momentum in the solar neighborhood comprises three distinct stellar populations. Two of the subgroups can be assigned to the accreted GSE stars and the heated population, respectively. The remaining subgroup is reminiscent of the GSS identified by An et al. (2023), as well as recent results predicted by numerical simulations.

We thank an anonymous referee for a careful review of this paper, which has improved the clarity of its presentation. Y.S.L. acknowledges support from the National Research Foundation (NRF) of Korea grant funded by the Ministry of Science and ICT (NRF-2021R1A2C1008679). Y.S.L. also gratefully






acknowledges partial support for his visit to the University of Notre Dame from OISE-1927130: The International Research Network for Nuclear Astrophysics (IReNA), awarded by the US National Science Foundation. Y.K.K. acknowledges support from Basic Science Research Program through the NRF of Korea funded by the Ministry of Education (NRF-2021R1A6A3A01086446). T.C.B. acknowledges partial support for this work from grant PHY 14-30152; Physics Frontier Center/JINA Center for the Evolution of the Elements (JINACEE), awarded by the U.S. National Science Foundation. D.A. acknowledges support provided by the National Research Foundation (NRF) of Korea grant funded by the Ministry of Science and ICT (No. 2021R1A2C1004117).

Funding for the Sloan Digital Sky Survey IV has been provided by the Alfred P. Sloan Foundation, the U.S. Department of Energy Office of Science, and the Participating Institutions. SDSS-IV acknowledges support and resources from the Center for High Performance Computing at the University of Utah. The SDSS website is [www.sdss.org](http://www.sdss.org).

SDSS-IV is managed by the Astrophysical Research Consortium for the Participating Institutions of the SDSS Collaboration, including the Brazilian Participation Group, the Carnegie Institution for Science, Carnegie Mellon University, Center for Astrophysics | Harvard & Smithsonian, the Chilean Participation Group, the French Participation Group, Instituto de Astrofísica de Canarias, The Johns Hopkins University, Kavli Institute for the Physics and Mathematics of the Universe (IPMU)/University of Tokyo, the Korean Participation Group, Lawrence Berkeley National Laboratory, Leibniz Institut für Astrophysik Potsdam (AIP), Max-Planck-Institut für Astronomie (MPIA Heidelberg), Max-Planck-Institut für Astrophysik (MPA Garching), Max-Planck-Institut für Extraterrestrische Physik (MPE), National Astronomical Observatories of China, New Mexico State University, New York University, University of Notre Dame, Observatório Nacional/MCTI, The Ohio State University, Pennsylvania State University, Shanghai Astronomical Observatory, United Kingdom Participation Group, Universidad Nacional Autónoma de México, University of Arizona, University of Colorado Boulder, University of Oxford, University of Portsmouth, University of Utah, University of Virginia, University of Washington, University of Wisconsin, Vanderbilt University, and Yale University.

The Guoshoujing Telescope (the Large Sky Area Multi-Object Fiber Spectroscopic Telescope, LAMOST) is a National Major Scientific Project that was built by the Chinese Academy of Sciences, funded by the National Development and Reform Commission, and operated and managed by the National Astronomical Observatories, Chinese Academy of Sciences.

### ORCID iDs

Ayeon Lee  <https://orcid.org/0000-0002-6570-3490>  
 Young Sun Lee  <https://orcid.org/0000-0001-5297-4518>  
 Young Kwang Kim  <https://orcid.org/0000-0002-6411-5857>  
 Timothy C. Beers  <https://orcid.org/0000-0003-4573-6233>  
 Deokkeun An  <https://orcid.org/0000-0002-8072-7511>

### References

Abdurro'uf, Accetta, K., Aerts, C., et al. 2022, *ApJS*, 259, 35  
 Allende Prieto, C., Sivarani, T., Beers, T. C., et al. 2008, *AJ*, 136, 2070  
 Amarante, J. A. S., Beraldo e Silva, L., Debattista, V. P., & Smith, M. C. 2020, *ApJL*, 891, L30  
 An, D., & Beers, T. C. 2020, *ApJ*, 897, 39

An, D., & Beers, T. C. 2021, *ApJ*, 907, 101  
 An, D., & Beers, T. C. 2021, *ApJ*, 918, 74  
 An, D., Beers, T. C., Lee, Y. S., et al. 2023, arXiv:2210.07542  
 Beers, T. C., Chiba, M., Yoshii, Y., et al. 2000, *AJ*, 119, 2866  
 Beers, T. C., Carollo, D., Ivezić, Ž., et al. 2012, *ApJ*, 746, 34  
 Belokurov, V., Erkal, D., Evans, N. W., et al. 2018, *MNRAS*, 478, 611  
 Belokurov, V., Sanders, J. L., Fattahi, A., et al. 2020, *MNRAS*, 494, 3880  
 Bennett, M., & Bovy, J. 2019, *MNRAS*, 482, 1417  
 Bland-Hawthorn, J., & Gerhard, O. 2016, *ARA&A*, 54, 529  
 Blanton, M. R., Bershady, M. A., Abolfathi, B., et al. 2017, *AJ*, 154, 28  
 Bonaca, A., Conroy, C., Wetzel, A., Hopkins, P. F., & Keres, D. 2017, *ApJ*, 845, 101  
 Brook, C. B., Kawata, D., Gibson, B. K., & Freeman, K. C. 2004, *ApJ*, 612, 894  
 Brook, C., Richard, S., Kawata, D., Martel, H., & Gibson, B. K. 2007, *ApJ*, 658, 60  
 Brook, C. B., Stinson, G. S., Gibson, B. K., et al. 2012, *MNRAS*, 426, 690  
 Buck, T. 2020, *MNRAS*, 491, 5435  
 Buder, S., Sharma, S., Kos, J., et al. 2021, *MNRAS*, 506, 150  
 Chambers, K. C., Magnier, E. A., Metcalfe, N., et al. 2016, arXiv:1612.05560  
 Chiba, M., & Beers, T. C. 2000, *AJ*, 119, 2843  
 Dawson, K. S., Schlegel, D. J., Ahn, C. P., et al. 2013, *AJ*, 145, 10  
 Deason, A. J., Belokurov, V., Koposov, S. E., & Lancaster, L. 2018, *ApJL*, 862, L1  
 De Silva, G. M., Freeman, K. C., Bland-Hawthorn, J., et al. 2015, *MNRAS*, 449, 2604  
 Dillamore, A. M., Belokurov, V., Font, A. S., & McCarthy, I. G. 2022, *MNRAS*, 513, 1867  
 Di Matteo, P., Haywood, M., Lehnert, M. D., et al. 2019, *A&A*, 632, A4  
 Fernández-Alvar, E., Fernández-Trincado, J. G., Moreno, E., et al. 2019, *MNRAS*, 487, 1462  
 Gaia Collaboration, Brown, A. G. A., Vallenari, A., et al. 2016, *A&A*, 595, A2  
 Gaia Collaboration, Brown, A. G. A., Vallenari, A., et al. 2018, *A&A*, 616, A1  
 Gaia Collaboration, Brown, A. G. A., Vallenari, A., et al. 2021, *A&A*, 649, A1  
 Gaia Collaboration, Vallenari, A., Brown, A. G. A., et al. 2022, arXiv:2208.00211  
 Gallart, C., Bernard, E. J., Brook, C. B., et al. 2019, *NatAs*, 3, 932  
 Grand, R. J. J., Bustamante, S., Gómez, F. A., et al. 2018, *MNRAS*, 474, 3629  
 Grand, R. J. J., Kawata, D., Belokurov, V., et al. 2020, *MNRAS*, 497, 1603  
 Han, D. R., Lee, Y. S., Kim, Y. K., & Beers, T. C. 2020, *ApJ*, 896, 14  
 Hawkins, K., Jofré, P., Masseron, T., & Gilmore, G. 2015, *MNRAS*, 453, 758  
 Haywood, M., Di Matteo, P., Lehnert, M. D., et al. 2018, *ApJ*, 863, 113  
 Helmi, A., Babusiaux, C., Koppelman, H. H., et al. 2018, *Natur*, 563, 85  
 Henden, A. A., Levine, S., Terrell, D., et al. 2018, AAS Meeting Abstracts, 232, 223.06  
 Horta, D., Schiavon, R. P., Mackereth, J. T., et al. 2021, *MNRAS*, 500, 1385  
 Kawata, D., Bovy, J., Matsunaga, N., & Baba, J. 2019, *MNRAS*, 482, 40  
 Kim, C., Lee, Y. S., Beers, T. C., et al. 2022, *JKAS*, 55, 23  
 Kim, Y. K., Lee, Y. S., & Beers, T. C. 2019, *ApJ*, 882, 176  
 Kwang Kim, Y., Sun Lee, Y., Beers, T. C., & Koo, J.-R. 2021, *ApJL*, 911, L21  
 Koo, J.-R., Sun Lee, Y., Park, H.-J., Kwang Kim, Y., & Beers, T. C. 2022, *ApJ*, 925, 35  
 Koppelman, H. H., Helmi, A., Massari, D., Price-Whelan, A. M., & Starkenburg, T. K. 2019, *A&A*, 631, L9  
 Kruijssen, J. M. D., Pfeffer, J. L., Reina-Campos, M., Crain, R. A., & Bastian, N. 2019, *MNRAS*, 486, 3180  
 Lee, Y. S., Beers, T. C., Sivarani, T., et al. 2008a, *AJ*, 136, 2022  
 Lee, Y. S., Beers, T. C., Sivarani, T., et al. 2008b, *AJ*, 136, 2050  
 Lee, Y. S., Beers, T. C., Allende Prieto, C., et al. 2011a, *AJ*, 141, 90  
 Lee, Y. S., Beers, T. C., An, D., et al. 2011b, *ApJ*, 738, 187  
 Lee, Y. S., Beers, T. C., Masseron, T., et al. 2013, *AJ*, 146, 132  
 Lee, Y. S., Beers, T. C., Carlin, J. L., et al. 2015, *AJ*, 150, 187  
 Lindegren, L., Klioner, S. A., Hernández, J., et al. 2021, *A&A*, 649, A2  
 Luo, A.-L., Zhao, Y.-H., Zhao, G., et al. 2015, *yCat*, 5146, 0  
 Luo, A.-L., Zhao, Y.-H., Zhao, G., et al. 2019, *yCat*, 5164, 0  
 Mackereth, J. T., Crain, R. A., Schiavon, R. P., et al. 2018, *MNRAS*, 477, 5072  
 Mackereth, J. T., Schiavon, R. P., Pfeffer, J., et al. 2019, *MNRAS*, 482, 3426  
 Majewski, S. R., Schiavon, R. P., Frinchaboy, P. M., et al. 2017, *AJ*, 154, 94  
 Myeong, G. C., Evans, N. W., Belokurov, V., Sanders, J. L., & Koposov, S. E. 2018, *MNRAS*, 478, 5449  
 Myeong, G. C., Vasiliev, E., Iorio, G., Evans, N. W., & Belokurov, V. 2019, *MNRAS*, 488, 1235  
 Myeong, G. C., Vasiliev, E., Aguado, D. S., et al. 2022, *ApJ*, 938, 21  
 Naidu, R. P., Conroy, C., Bonaca, A., et al. 2020, *ApJ*, 901, 48  
 Necib, L., Ostdiek, B., Lisanti, M., et al. 2020, *NatAs*, 4, 1078  
 Nissen, P. E., & Schuster, W. J. 2010, *A&A*, 511, L10

- Onken, C. A., Wolf, C., Bessell, M. S., et al. 2019, *PASA*, 1512, e033
- Re Fiorentin, P., Spagna, A., Lattanzi, M. G., & Cignoni, M. 2021, *ApJL*, 907, L16
- Rockosi, C. M., Sun Lee, Y., Morrison, H. L., et al. 2022, *ApJS*, 259, 60
- Schönrich, R., Binney, J., & Dehnen, W. 2010, *MNRAS*, 403, 1829
- Smolinski, J. P., Lee, Y. S., Beers, T. C., et al. 2011, *AJ*, 141, 89
- Wang, J., Shi, J., Zhao, Y., et al. 2016, *MNRAS*, 456, 672
- Xiang, M., Ting, Y.-S., Rix, H.-W., et al. 2019, *ApJS*, 245, 34
- Yanny, B., Rockosi, C., Newberg, H. J., et al. 2009, *AJ*, 137, 4377
- York, D. G., Adelman, J., Anderson, J. E., Jr., et al. 2000, *AJ*, 120, 1579
- Yuan, Z., Myeong, G. C., Beers, T. C., et al. 2020, *ApJ*, 891, 39
- Zhao, G., & Chen, Y. 2021, *SCPMA*, 64, 239562